OCEANOGRAPHY

Ekman revisited: Surface currents to the left of the winds in the Northern Hemisphere

Michael J. McPhaden[1]*, K. Athulya[2,3], M. S. Girishkumar[2], Mirko Orlić[4]

Ekman's theory of wind-driven ocean currents on a rotating planet is central to our understanding of why surface currents are deflected to the right of the winds in the Northern Hemisphere and to the left of the winds in the Southern Hemisphere. The theory admits solutions for currents deflected in the opposite direction at periods shorter than the local inertial period, but Ekman did not mention these currents, and they have only rarely been observed. Here, we describe a prominent example of surface flow in the Bay of Bengal directed to the left of clockwise-rotating land breeze wind forcing using multiple years of data from a long-term deepwater surface moored buoy. We further refine Ekman's theory so as to better reconcile it with our own and previous measurements and then conclude by discussing the broad implications of this work for understanding wind-forced ocean circulation.

INTRODUCTION

Vagn Walfrid Ekman's 1905 theory (*1*) describing the influence of the Earth's rotation on wind-driven ocean currents is one of the foundational principles of modern oceanography. Virtually all practicing oceanographers know that currents in a frictional boundary layer rotate to the right of the surface winds in the Northern Hemisphere and to the left of the surface winds in the Southern Hemisphere. The essential aspects of this theory, including how near-surface currents spiral with depth in response to wind forcing, have been validated with modern observational techniques in many areas of the world ocean over the past several decades (*2*–*9*).

Ekman in his seminal paper dismissed an earlier theory for wind-driven flow proposed by Zoeppritz (*10*) who neglected the Earth's rotation and assumed that friction in the ocean was governed by molecular-scale processes. The latter implied that the ocean would equilibrate to wind forcing only after hundreds to thousands of years, which was not consistent with contemporary observations suggesting that currents adjusted to changing winds with a delay of only a day or two. Ekman realized that these short adjustment times required vertical viscosities in the ocean orders of magnitude larger than molecular viscosity, which he inferred were likely governed by macroscale "vortices."

Ekman wrote down the full equations for time-dependent flow but only solved for steady and transient motion. However, at superinertial frequencies much higher than the Coriolis frequency (i.e., $\omega >> f = 2\Omega\sin\theta$, where Ω is the Earth's rotation rate and θ is latitude), Zoeppritz's theory of periodic motion is formally correct and, allowing for realistic values of eddy viscosity, admits a range of solutions where, under certain conditions, wind-driven ocean currents turn to the left of the wind in the Northern Hemisphere (*11*). In a few notable instances, such superinertial motions in the ocean have been observed (*4*, *6*, *7*, *12*–*15*). However, the energetic background continuum of internal waves (*4*) and submesoscale (*9*, *16*, *17*) and other small-scale processes can easily obscure them, making detection difficult. Thus, compared to the vast literature on inertial oscillations and applications of classical Ekman dynamics (*18*, *19*), studies of wind-driven superinertial flow to the left of the winds are rare.

Here, we present evidence for very prominent superinertial oscillations directed to the left of the surface winds in the western Bay of Bengal. These oscillations are forced by a regular diurnal land breeze system (*20*) that extends hundreds of kilometers offshore from the east coast of India during the June to September southwest monsoon (*21*). The regularity of the diurnal forcing at low latitudes represents a narrow frequency band forcing that produces a highly organized narrow band response in the ocean, which is well separated from the inertial period. The signal clearly stands out well above the background noise, which is reduced by the multiple years of high–temporal and vertical resolution time series data available from an open-ocean deepwater mooring to define the forcing and response. The clarity of the wind forcing and the ocean response both at and below the ocean surface thus provides a unique opportunity to explore aspects of wind forced ocean circulation that, with the few exceptions noted above, have largely been ignored in the scientific literature since the time of Ekman. Our analysis supports the theory of wind-forced ocean currents that Zoeppritz first proposed in 1878, nearly 30 years before Ekman published his seminal paper, taking into account that turbulence is the source of frictional drag in the ocean.

RESULTS

Land breeze system in the Bay of Bengal

In coastal regions, differential heating of the land and ocean over the course of a day typically results in onshore flow during daylight hours when the land is warmer and offshore flow during nighttime when the land is cooler. The diurnal "land breeze system" (*20*) over the ocean is particularly pronounced in the southwestern Bay of Bengal (between 10°N and 15°N) where its offshore extent is seasonally modulated by the component of monsoon winds perpendicular to shore (*21*). In December to January during the northeast monsoon, for example, the onshore component of the large-scale winds confines the land breeze to only about 50 km from the coast in the southwestern Bay of Bengal (Fig. 1A). In contrast, during July to August, large-scale westerly winds associated with the southwest monsoon extend the land breeze 400 to 500 km offshore (Fig. 1B). The amplitude of this diurnal land breeze is 1 to 2 m s^{-1} (*20*, *21*), covering up to 20% of the Bay of Bengal in July to August when it accounts for 15% of the total wind speed magnitude (*21*).

[1]NOAA/Pacific Marine Environmental Laboratory, Seattle, Washington, USA. [2]Ministry of Earth Sciences, Indian National Centre for Ocean Information Services (INCOIS), Hyderabad, India. [3]School of Ocean Science and Technology, Kerala University of Fisheries and Ocean Studies, Cochin, India. [4]University of Zagreb, Faculty of Science, Andrija Mohorovičić Geophysical Institute, Zagreb, Croatia.
*Corresponding author. Email: michael.j.mcphaden@noaa.gov

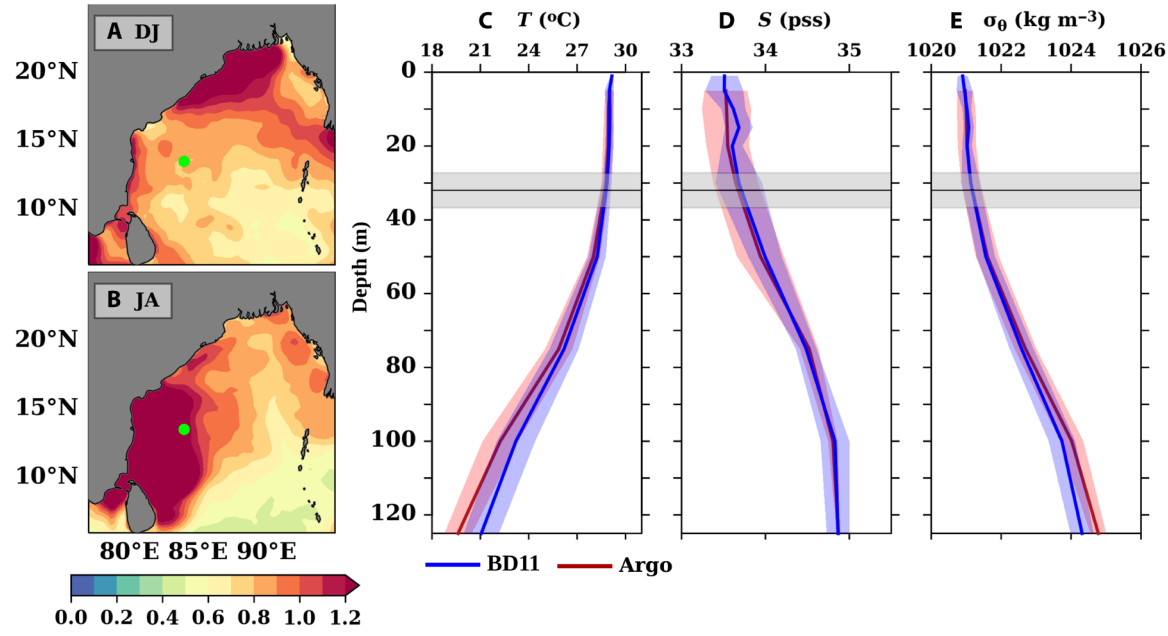

Fig. 1. Background conditions in the Bay of Bengal. Diurnal amplitude estimates of CCMP 6-hourly wind speed (m s^{-1}) based on data from 2010–2019 during (**A**) December to January (DJ) and (**B**) July to August (JA). The diurnal amplitude of wind speed during every month is estimated separately from 2010 to 2019, and its average values for December to January and July to August are presented in (A) and (B), respectively. The diurnal amplitude values are significantly different from zero at the 95% confidence level at every grid point based on the application of a *t* test. The green circle represents the location of the open-ocean moored buoy (BD11) at 13.5°N, 84.0°E. Vertical profiles of hydrographic conditions at the buoy (**C** to **E**) showing the mean (thick line) and one SD (shading) of (C) temperature (*T*; °C), (D) salinity [*S*; in practical salinity scale (pss)], and (E) density (σ_θ; kg m^{-3}) derived from buoy data (blue) and nearby gridded Argo data (red) during July to August based on an average over 6 years (2011, 2013, 2014, 2017, 2018, and 2019). The mean mixed layer depth determined from Argo, defined as the depth at which density increases by 0.125 kg m^{-3} from the surface, is shown as a black horizontal line in (C) to (E) with ± two SE uncertainly limits in shading. This estimate is 32.5 ± 4.7 m. The equivalent estimate using the moored buoy data (not shown in the graphic for clarity) is 36.4 ± 5.8 m. Given the uncertainties in these estimates, they are essentially statistically equivalent.

The land breeze extends far enough offshore during July to August to encompass the position of a heavily instrumented open-ocean surface moored buoy maintained at 13.5°N, 84.0°E for nearly a decade (Fig. 1, A and B). The mean surface mixed layer at this location is about 30 m deep, below which a strongly stratified thermocline and pycnocline is found (Fig. 1, C to E). The mean hydrographic structure at the buoy location is similar to that inferred from Argo floats within 1° latitude and longitude of the buoy.

The buoy is located in a region characterized by a strong external and internal semidiurnal tides but no appreciable diurnal tides (fig. S1). We will show that the strong diurnal ocean currents within and extending below the mixed layer at this location (fig. S2) are forced by the diurnal land breeze. These currents oscillate at superinertial periods because, at the latitude of mooring, the diurnal period is much shorter than and well separated from the inertial period of 49.6 hours (fig. S2). Land breeze variations in the Bay of Bengal during July to August rotate clockwise (CW; fig. S3), consistent with previously reported satellite and in situ observations (*20*, *21*). This CW sense of rotation in the Bay of Bengal is determined by the combined effects of the Coriolis force, thermally induced cross-shore pressure gradient in the atmospheric boundary layer, and synoptic-scale pressure gradients (*22*–*25*).

Hourly observations from the mooring were band-pass filtered around the diurnal cycle and averaged across July to August for 6 years between 2011 and 2019 to generate a composite of diurnally evolving surface wind and ocean velocity. The band-passed velocity data exhibit very sizeable (±6 cm s^{-1}) variations that rotate in a CW direction like the surface wind stress but deflected to the left of the wind stress throughout the day (Fig. 2A). Diurnal surface currents observed from coastal radar data closer to shore behave in a similar way, rotating CW with a deflection to the left of the surface winds (*21*).

Superinertial flow to the left of the winds

We hypothesize that the diurnal period currents rotating to the left of the winds in the Bay of Bengal are consistent with a generalized Ekman theory for superinertial flow in a constant density ocean (*11*, *26*). Ekman solved the problem for steady-state forcing (i.e., $\omega = 0$) and transient wind-forced flow, focusing on subinertial periods where the currents spiral to the right of the winds in the Northern Hemisphere. The same equations that Ekman used, but solved for the full range of frequencies on rotating planet (Materials and Methods), predict that subinertial flow ($\omega < f$) in the Northern Hemisphere is always deflected to the right of the winds, whereas superinertial flow ($\omega > f$) is directed to the right of counterclockwise (CCW)–rotating winds but to the left of CW-rotating winds.

Both subinertial and superinertial flows spiral with depth on vertical scales (D, D_1, and D_2) that depend on the value of the eddy viscosity (K) assumed to be constant. Specifically

$$D = \pi\sqrt{\frac{2K}{f+\omega}}, D_1 = \pi\sqrt{\frac{2K}{f-\omega}}, D_2 = \pi\sqrt{\frac{2K}{\omega-f}}$$

where D is related to CCW rotation at all frequencies, D_1 to CW rotation at subinertial frequencies, and D_2 to CW rotation at superinertial frequencies (Materials and Methods, Eq. 7C). The shape of the spiral

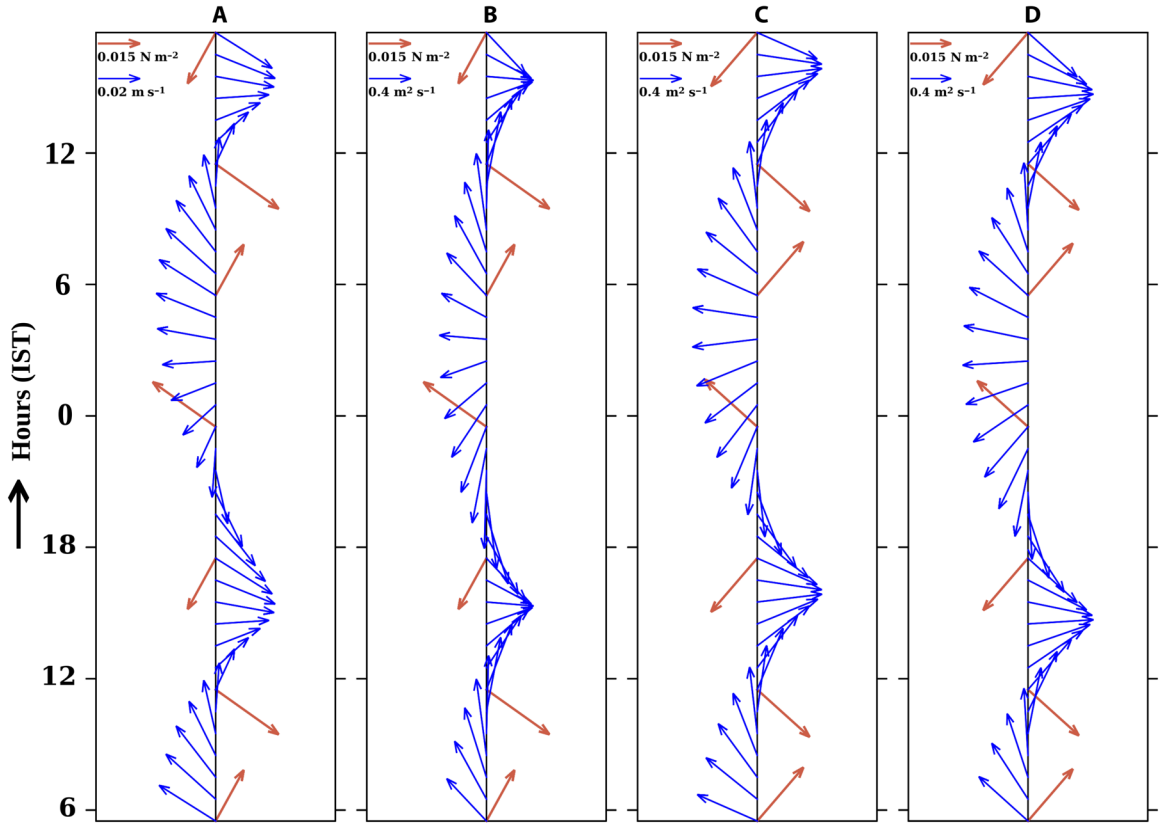

Fig. 2. Currents deflected to the left of CW-rotating surface wind stress. Composite hourly band-pass–filtered (22.5 to 25.5 hours) BD11 mooring data in July to August for (**A**) wind stress vectors (red; N m^{-2}) and surface current vectors (blue; m s^{-1}), (**B**) wind stress vectors (red; N m^{-2}) and 30-m depth-integrated current vectors (blue; m^2 s^{-1}), (**C**) CW component of wind stress vectors (red; N m^{-2}) and 30-m depth-integrated CW component of current vectors (blue; m^2 s^{-1}), and (**D**) CW component of wind stress vectors (red; N m^{-2}) and theoretical depth-integrated current vectors (blue; m^2 s^{-1}) estimated from observed CW component of wind stress using Eq. 6 (Materials and Methods). For better readability, the *y* axis is repeated for a half-day and the wind vectors in (A) to (D) are shown only every 6 hours. The analysis was carried out for each of 6 years individually (2011, 2013, 2014, 2017, 2018, and 2019) and then averaged to obtain composite current and wind stress vectors in the diurnal period band. IST, Indian Standard Time.

depends on the depth of the water column (h) relative to D, D_1, and D_2. The eddy viscosity is generally poorly constrained by observations, but a vertical integral over the depth of the frictional flow is independent of K. For wind stress variations at a frequency ω of the form

$$\tau = A\exp(i\omega t) + B\exp(-i\omega t)$$

where t is time and A and B are constants, depth-integrated horizontal currents (or equivalently, volume transport per unit width, simply referred to as volume transport hereafter) will follow the expression (see Materials and Methods, Eq. 6)

$$V = \frac{A}{i\rho(f+\omega)}\exp(i\omega t) + \frac{B}{i\rho(f-\omega)}\exp(-i\omega t)$$

Depending on the relative size of the constants A and B, the wind stress rotates CW ($A < B$), is linearly polarized ($A = B$), or rotates CCW ($A > B$). The theory thus predicts that volume transport is 90° to the right of the wind in the Northern Hemisphere, independent of turbulent eddy viscosity, except for CW-rotating superinertial winds ($A < B$) for which the volume transport is directed 90° to the left of the winds.

In our data, the vertical integral of the flow over the 30 m mixed layer depth shows an angle of deflection to the left of the winds of roughly 90°, varying between 73° and 103° depending on the time of day (Fig. 2B and fig. S4B). This time variable rate of deflection is due to the fact that, although the winds are dominated by CW rotation (fig. S3), a rotary spectrum decomposition (*4*, *12*, *27*) indicates that there is a small CCW component as well, i.e., $A \neq 0$ although $A << B$ (Fig. 3A). Below, we will focus on just the CW component flow because the theory is linear and allows us to separate CW and CCW components and because the very large signal-to-noise ratio in the CW component offers the clearest and most compelling comparison with the theory.

Comparison of observations and theory

For comparison of the observations with theory, we choose 30 m as the depth of integration for a variety of reasons. First, the surface mixed layer is about 30 m deep at the mooring location (Fig. 1, C to E). Second, rotary spectra show that, like the wind stress, the locally wind-forced diurnal period current response in the upper 30 m is dominated by CW flow (Figs. 3C and 4). The depth-integrated flow in the upper 30-m mixed layer is almost identical to the depth-integrated flow of just the CW component (cf. Fig. 2, B and C). Lastly, the root-mean-square difference (RMSD) between the observed flow and the theoretically expected flow as a

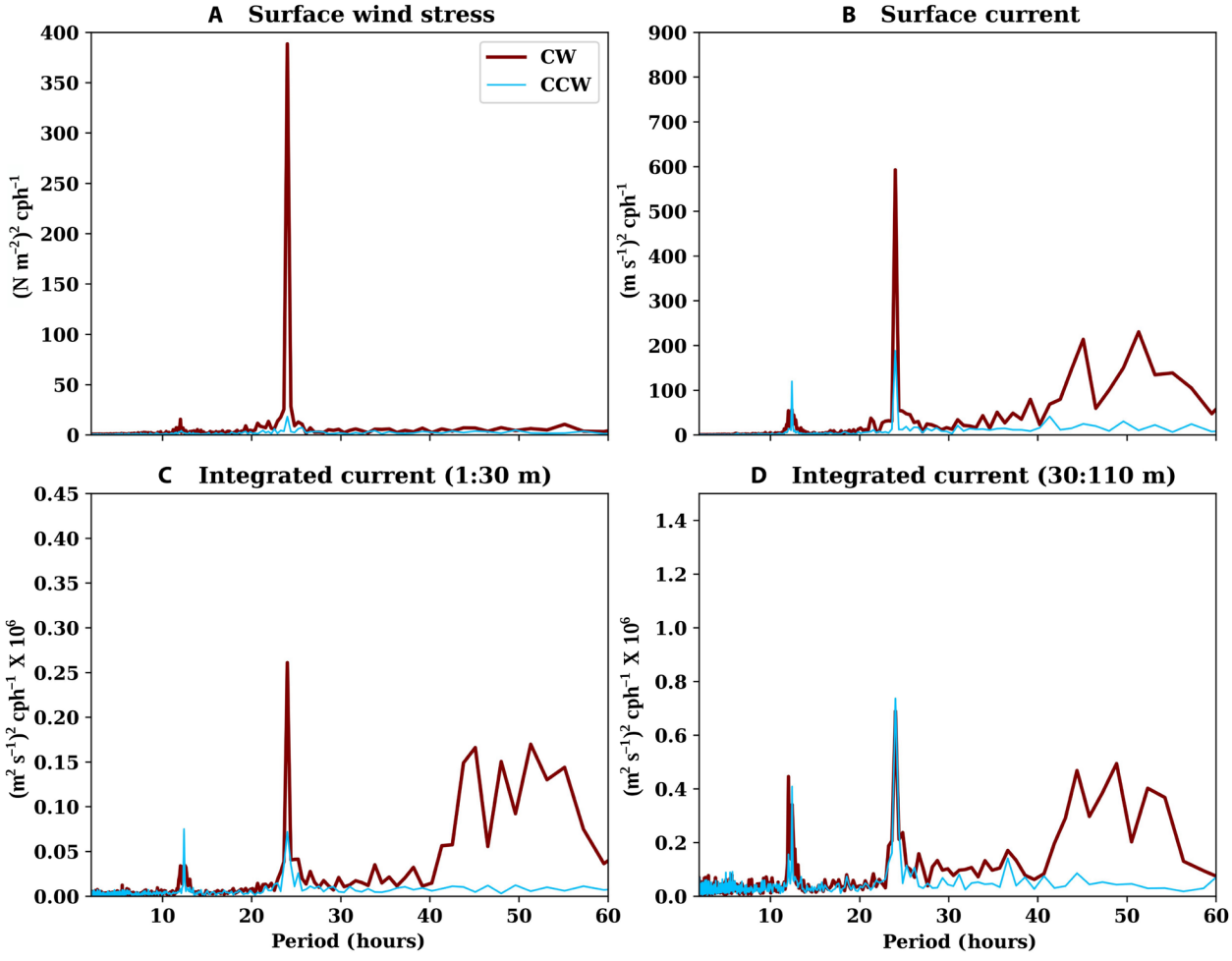

Fig. 3. Rotary spectra of surface wind stress and ocean currents based on July to August mooring data. Rotary spectra (CW in maroon and CCW in cyan) of (**A**) surface wind stress [(N m^{-2})^2 cph^{-1}], (**B**) surface current speed [(m s^{-1})^2 cph^{-1}], (**C**) 30-m integrated current speed [(m^2 s^{-1})^2 cph^{-1}], and (**D**) current speed integrated over depth of 30 to 110 m [(m^2 s^{-1})^2 cph^{-1}] during July to August derived from BD11 mooring data at 13.5°N, 84.0°E. Rotary spectra are based on the average of estimates from six individual years (2011, 2013, 2014, 2017, 2018, and 2019). Spectral estimates are plotted without band averaging; period (in hours) is shown on the *x* axis.

function of the depth over which the currents are integrated shows a minimum at 30 m (fig. S5).

There is a notable visual correspondence between the observed depth-integrated CW flow at the mooring site and that predicted by theory (cf. Fig. 2, C and D). A more quantitative comparison of the theory and the observations for the CW component of depth-integrated flow (Fig. 5B) shows an approximate 108° mean deflection of the flow to the left of the surface wind stress (larger than the predicted 90° from theory) and a velocity amplitude nearly equal to the corresponding theoretical value. Given the 95% confidence limits for these estimates, however, they are close to theoretical expectations.

The agreement between the observations and the theory is less obvious for the surface currents if one considers the usual case of a surface layer much deeper than the characteristic depths of the flow (i.e., $h >> D$, D_1, and D_2). This is the parameter range in which Ekman solved for steady flow ($\omega = 0$) and found that the currents rotate 45° to the right of the wind stress in the Northern Hemisphere. In this parameter range, the theory also predicts a 45° surface deflection for superinertial flow ($\omega >> f$) but to the left of CW-rotating winds (Materials and Methods, Eq. 8B). However, the observed surface currents rotate closer to 90° to the left of the winds, which is significantly different than expected from theory for $h >> D$, D_1, and D_2 (Fig. 2A and fig. S4A).

In contrast, much better agreement between the observed surface currents and theory is achieved in a parameter range where the characteristic depths of superinertial current variations are much larger than the depth of the surface layer (specifically, $h << D$ and D_2). This situation applies when there is intense vertical mixing in a shallow constant density surface layer of depth h resting atop a strongly stratified thermocline wherein vertical mixing is much weaker. Horizontal surface velocity, v, is then given by (Materials and Methods, Eq. 9B)

$$v = \frac{A}{\rho h(f+\omega)}\exp\left[i\left(\omega t - \frac{\pi}{2}\right)\right] + \frac{B}{\rho h(\omega - f)}\exp\left[-i\left(\omega t - \frac{\pi}{2}\right)\right]$$

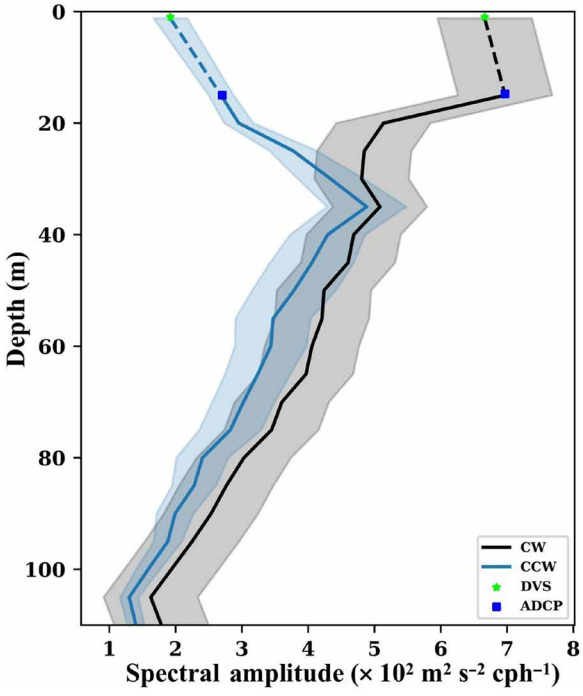

Fig. 4. Vertical profiles of rotary spectra components based on BD11 mooring data. Profile of rotary spectra amplitude (× 10^2 m^2 s^{-2} cph^{-1}) for CW (black) and CCW (blue) components of current velocity at a period of 24 hours from the mooring at 13.5°N, 84.0°E during July to August. Green stars denote the 1 m measurement depth of a Doppler volume current sampler (DVS), and blue squares represent the 15 m depth below which acoustic Doppler current profiler (ADCP) data are available. The dashed line indicates interpolated values between DVS and ADCP. Shading represents two SEs estimated using a bootstrap method. Rotary spectra are based on the average of estimates for six individual years (2011, 2013, 2014, 2017, 2018, and 2019).

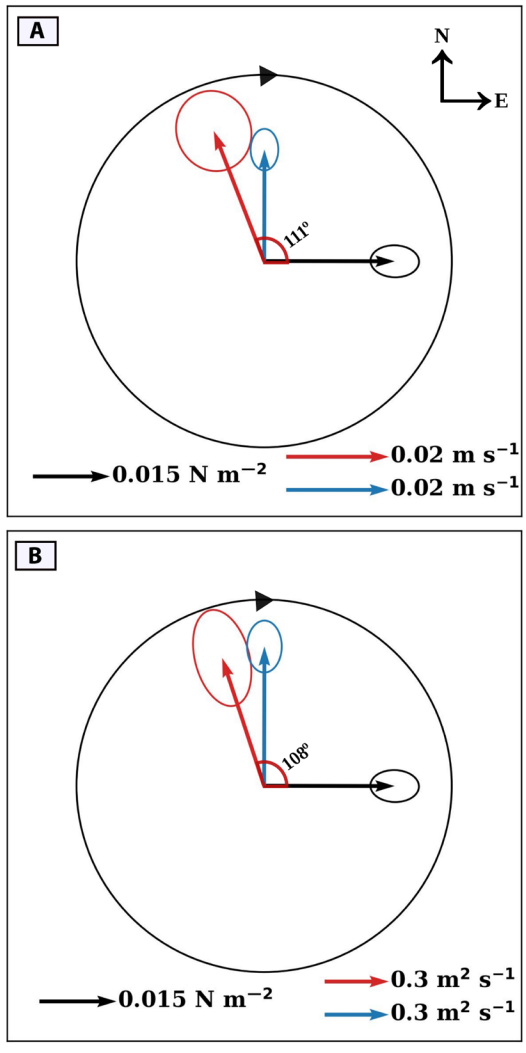

Fig. 5. Snapshot at 1000 IST of observed and theoretical currents directed to the left of CW-rotating diurnal surface wind stress. Wind stress vectors (black) and current vectors (observations in red and theory in blue) rotate CW in fixed relation to one another, making one complete rotation in a 24-hour period. (**A**) CW component of the observed surface current vector (m s^{-1}) and theoretical surface current vector (m s^{-1}) estimated from the CW component of wind stress (N m^{-2}) using Eq. 9B (Materials and Methods), with a value of 30 m prescribed for *h*; (**B**) CW component of the 30-m depth-integrated observed current vector (m^2 s^{-1}) and depth-integrated theoretical current vectors (m^2 s^{-1}) estimated using Eq. 6 (Materials and Methods) forced by the observed CW component of wind stress. The angle between the wind stress vector and current vector is 111° in (A) and 108° in (B). Ellipses represent two SEs for vector magnitudes and orientations estimated on the basis of deviations from the mean zonal and meridional current components using a bootstrap method. These ellipses almost overlap for the observed and theoretical currents. The diurnal (22.5 to 25.5 hours) amplitude of the CW rotary coefficient for wind stress vectors and current vectors during July to August is estimated separately for six individual years (2011, 2013, 2014, 2017, 2018, and 2019) and then averaged to reconstruct the CW component of current vectors, wind vectors, and error ellipses in the diurnal period band.

The theory in this limit presumes that all the momentum input by the surface winds is trapped in the layer of depth h above the thermocline and that the superinertial surface currents are depth independent in this layer. The equation above shows that, for CW-rotating winds with $A = 0$, currents are deflected 90° to the left of the winds, in much better agreement with the observations (Fig. 5A). Note that the expression for v above, when multiplied by h, is identical to the volume transport equation for V, i.e., $V = vh$, which explains the similarity between the surface current and the transport responses to wind forcing that we observe (Fig. 5).

We can obtain a third estimate for h from the ratio V/v for comparison with estimates from the density field (Fig. 1, C to E) and from minimizing the differences between observed and theoretical depth-integrated flow (fig. S5). Using the observed vector lengths in Fig. 5 (and ignoring their small angular difference relative to the winds) yields a value of $h = 23 \pm 21$ m, where the two-SE estimate takes into account the uncertainties in both V and v. The value of h computed this way is smaller than 30 m, but it cannot be distinguished statistically from 30 m with 95% confidence.

In the limit of slab-like flow described above, the value of K must be sufficiently large in order for $D_2 >> h$. We can estimate K by making no assumptions about what parameter range the observations fall in, using Eq. 7B in Materials and Methods. We first compute theoretical currents using the observed wind stress for various values of K as a function of depth within the 30-m-thick mixed layer. We then compute the RMSD between the theoretical currents and the observed currents (fig. S6) and find that minima in RMSD in the upper 30 m occur for the largest values of K, i.e., $K \approx 10^{-1}$ m^2 s^{-1} or larger. In this limit, the theory does not provide much discriminating

power to identify a preferred value of K, other than that it must be very large in the mixed layer and abruptly change to a much lower value in the thermocline. Similarly, large values of K (~0.5 × 10^{-1} m^2 s^{-1}) were required to reconcile the observed vertical structure and deflection of near-inertial mixed layer currents relative to the winds in a 50-m-thick mixed layer off the coast of California (*13*). An analysis of superinertial flow in Southern Hemisphere surface drifting buoy observations likewise found that the most successful model describing the observed variability was one in which the mixed layer was O(30 to 50 m) deep and in which the eddy viscosity was constant between about 0.4 × 10^{-1} m^2 s^{-1} to 1.2 × 10^{-1} m^2 s^{-1} (*15*). We note that, for K ~ 10^{-1} m^2 s^{-1}, the relevant frictional depth at the diurnal period (D_2) is 225 m, which is almost eight times larger than the mixed layer depth h at the mooring site. These results are consistent with representing superinertial flow in response to land breeze forcing as slab-like flow in a well-mixed surface layer according to the equation for v above.

DISCUSSION

Allowing for realistic values of eddy viscosity, our analysis supports Zoeppritz's 1878 theory for wind-forced ocean currents proposed nearly 30 years before Ekman published his seminal paper. Zoeppritz's theory is formally just a special case of Ekman's more general theory, applicable in the superinertial parameter range where $\omega >> f$. Ekman did not make this connection in his assessment of Zoeppritz's work, probably because he was more focused on the distinction between turbulent versus molecular viscosity in governing the ocean's response to wind forcing. He understood that reconciling theory with observations depends critically on the magnitude and structure of ocean mixing, an issue as relevant today as it was over 100 years ago.

The reason that the currents turn to the left of the CW-rotating surface winds is that, with $\omega >> f$, the dominant restoring force for the flow is turbulent friction. At superinertial periods, winds would tend to force surface currents downwind, but frictional drag on these flows delays their response. Thus, as the winds rotate in a CW direction, the lagging currents appear to be deflected to the left of the winds. This lag increases with depth resulting in the equivalent of an Ekman spiral when the mixed layer is much deeper than the characteristic depth of the frictional flow.

We can contrast conditions in July to August with those in December to January to support our hypothesis that CW-rotating surface currents deflected to the left of the CW-rotating land breeze represent wind-forced superinertial flow rather than some coincidental relationship between diurnal tides and winds. The land breeze does not extend offshore to the mooring site in the southwestern Bay of Bengal during December to January (Fig. 1A), and, consequently, the diurnal cycle in both surface wind forcing and ocean velocity in the upper ocean is absent (fig. S7). If diurnal tides were responsible for the observed diurnal current variations that we observe in July to August, then we would have expected to see a much stronger ocean velocity signal at 24-hour periods despite the absence of surface wind forcing in December to January. However, there are effectively no diurnal surface layer velocity variations in December to January, consistent with both the lack of significant wind forcing and the lack of a diurnal tidal signal at the buoy location as noted earlier (fig. S1).

The theory is formulated for constant density ocean so, strictly speaking, it applies only to the surface mixed layer. However, there is clearly superinertial flow in the thermocline with near isotropy between CW and CCW components when the diurnal wind forcing is strong in July to August (Fig. 4). It is likely that variability in the thermocline is generated by pressure work at the base of the mixed layer due to variations in vertical velocity related to spatial inhomogeneities in the land breeze system. Small spatial variations in the diurnal winds would produce wind-driven surface convergences and divergences that randomly pump the thermocline up and down, generating internal waves at the diurnal cycle that propagate superinertial flow downward into the thermocline. According to theory, internal waves that propagate energy downward exhibit upward phase propagation, which is evident below the mixed layer at diurnal periods, particularly in the zonal velocity component (fig. S8). Note that some superinertial energy at the mooring site could also be generated remotely as wind-forced near-inertial waves at higher latitudes that propagate energy equatorward, but this process is most relevant to variability much closer to the local inertial period than to the diurnal cycle.

It is likely that other low-latitude locations under the influence of land breeze forcing experience similar energetic superinertial flows as described here. We have detected similar flows from surface moored buoy data near 18°N during the northeast monsoon, when the diurnal land breeze extends hundreds of kilometers offshore in the northern Bay of Bengal (Fig. 1A). However, the signal is weaker there and complicated by stronger tidal signals. Nonetheless, the results of this study will be of value in helping to identify and dynamically interpret superinertial flows in other parts of the world ocean particularly those at low latitudes under the influence of land breeze forcing.

The results of this paper provide a valuable framework for interpreting data that will be collected from a proposed new NASA satellite mission to simultaneously measure surface winds and ocean currents over the global ocean with 5-km horizontal resolution and 12-hour temporal resolution (*28*, *29*). This mission was recommended by the 2018 US National Academies' Decadal Survey (*30*) to accurately determine of how air-sea interactions involving surface winds contribute to the generation of ocean waves, inertial oscillations, eddies, and large-scale ocean currents and how these variations, in turn, mediate ocean mixing both laterally and vertically. These processes are crucial to our understanding of weather and climate variations, marine biogeochemical cycles, ocean productivity, ecosystem dynamics, and marine fisheries. The satellite mission will also provide data for real-time applications such as search and rescue and oil spill response. The superinertial flows that we describe here will be a very prominent feature of the high frequency satellite retrievals particularly in the tropics where the inertial period is long and the ocean response to wind forcing is strong. Our results will help to clarify the dynamics of the high frequency variations observed by this new satellite within the context of the full spectrum of ocean forcing and response.

MATERIALS AND METHODS

Data sources and data processing

The measurements from a moored buoy (designated BD11) at 13.5°N, 84.0°E in the southwestern Bay of Bengal are the primary data used in the present study (*31*). The buoy is anchored in water depths of 3325 m, so measurements there represent open-ocean conditions. Measurements include wind velocity at 4 m height, near-surface

ocean current velocity measurements using a Doppler volume current sampler at a depth of around 1 m (nominally defined as surface current in the present study), and current profiles with 5 m vertical resolution from 15 to 115 m using a 150-kHz acoustic Doppler current profiler (ADCP). Subsurface temperature and salinity measurements are made at depths of 1, 5, 10, 15, 20, 30, 50, 75, 100, and 200 m. All the mooring measurements are made at 1-hour time intervals.

Buoy wind speed data were converted to 10 m height assuming logarithmically varying wind profiles under neutrally stable atmospheric conditions using the expressions

$$\mathbf{u} = \mathbf{u}(z_m)\frac{\ln(10/z_0)}{\ln(z_m/z_0)}, \mathbf{v} = \mathbf{v}(z_m)\frac{\ln(10/z_0)}{\ln(z_m/z_0)}$$

where $\mathbf{u}$ and $\mathbf{v}$ are zonal and meridional components of wind vectors at 10 m height, $\mathbf{u}(z_m)$ and $\mathbf{v}(z_m)$ are zonal and meridional components of wind vectors at the measurement height z_m, and z_0 is the roughness length in meters. A value of 2×10^{-4} m is prescribed for roughness length (*32*).

The wind stress τ at the ocean surface is then estimated as follows

$$|\tau| = \rho_{air} C_d(\mathbf{u}^2 + \mathbf{v}^2), \qquad \arg(\tau) = \tan^{-1}\frac{\mathbf{v}}{\mathbf{u}}$$

where ρ_{air} is the density of air (1.2 kg m^{-3}) and C_d is the drag coefficient that we set to 1.4×10^{-3}. In principle, one should compute stress using winds relative to the surface currents and a more sophisticated algorithm for the drag coefficient that incorporates atmospheric boundary layer stability, wind speed dependence, and cool skin-warm layer effects (*33*). Accounting for these differing effects leads to wind stresses that are nearly perfectly correlated (≥0.98) with our estimates and that differ in amplitude by only a few percent in the range of wind speeds that we encounter. These differences are much smaller than the uncertainties due to sampling error, which is the dominant source of error in our analysis, and they do not significantly affect our results. Moreover, using the COARE algorithm results in a one-third reduction in the number of wind stress estimates available to us, which leads to a significant increase in sampling error, because of missing concurrent meteorological data needed for the calculation. Thus, we opt for the simpler wind stress calculation to maximize the signal-to-noise in our analysis.

All observational analyses of mooring data are based on years 2011, 2013, 2014, 2017, 2018, and 2019. Data from 2012, 2015, and 2016 were discarded primarily due to suspicious velocity measurements as a result of malfunctioning ADCPs. Individual yearly analyses were then averaged to obtain composite winds, currents, and other variables in the diurnal period band.

Satellite-based Cross-Calibrated Multi-Platform (CCMP) version 3.0 wind vector data with 0.25° spatial resolution and 6-hour temporal resolution (*34*) are used to estimate spatial variations in the diurnal amplitude of wind speed as in Fig. 1 (A and B) using fast Fourier transform analysis methods.

Gridded temperature and salinity data with 1° spatial resolution and 10-day temporal resolution are derived from Argo profiles using a variational data interpolation methodology to describe climatological hydrographic conditions in the study region. These data are gridded at depths of 5, 10, 20, 30, 50, 75, 100, and 125 m in the upper 125 m (*35*).

We use the Welch averaged periodogram method (*36*) to document the existence of near-inertial current variability, with time series normalized by their SD before performing spectral analysis. The 95% confidence levels for spectra are estimated using *F* statistics of red-noise spectra based on lag 1 autocorrelations (*37*). CW and CCW components of the wind and current vectors are examined using rotary spectra as a function of frequency (*4*, *12*, *27*). All the analyses are presented in Indian Standard Time (5 hour and 30 min ahead of universal time). The statistical uncertainty of the mean for each parameter is presented as two SEs estimated on the basis of deviations from respective means using a bootstrap method (*32*).

The MITgcm tide model

We use three-dimensional Massachusetts Institute of Technology general circulation model (MITgcm) configuration (*38*) to study the internal tide characteristics over the western Bay of Bengal. The three-dimensional MITgcm (*39*) is a nonlinear, hydrostatic model that uses the Boussinesq approximation to solve the Navier-Stokes equations on an Arakawa C-grid. It has been configured to simulate the internal tides over the west coast of India in a domain that spans 12°N to 21.5°N and 78°E to 90°E. Horizontal resolution is around 1.6 km along shorelines, decreasing gradually toward the open ocean with a maximum value of 2.1 km in the zonal direction and 3.0 km in the meridional direction. A version of Earth Topography (ETOPO2) modified for shallow water regions of the Indian Ocean (*40*) is used for model bathymetry. The model has 23 vertical levels; vertical resolution in the upper 120 m is 10 m with a coarser resolution below. Horizontal and vertical eddy diffusivity are parameterized using standard methodologies (*41*, *42*). To initialize the model, monthly climatological temperature and salinity data with 0.25° horizontal resolution from World Ocean Atlas 2013 (WOA13) (*43*) are re-gridded to the model domain using bilinear interpolation. The model is forced using the Advanced Scatterometer daily wind stress data with 0.25° horizontal resolution and barotropic velocity component from the TOPEX/Poseidon global tidal model (*44*) along all the open boundaries of the model domain. The model surface layer is relaxed to Advanced Very High-Resolution Radiometer data with 0.25° horizontal resolution and sea surface salinity from the monthly climatology of WOA13 every 10 days. The model time step is 120 s. Model results, including for internal tides, have been successfully validated against observations (*38*).

Summary of theory

Governing equations

Here, we summarize highlights of Ekman theory of relevance to this study. Let us consider a constant density surface layer of the ocean. The origin of coordinate system is placed at the sea surface with the *z* axis pointing vertically upward and the domain of interest extending from the base of the surface layer ($z = -h$) to the sea surface ($z = 0$). If the wind is uniform in space and the sea is horizontally unbounded, then the horizontal pressure gradient vanishes and motion is uniform in the horizontal direction. The linearized momentum equation is then

$$\frac{\partial v}{\partial t} + ifv = K\frac{\partial^2 v}{\partial z^2} \tag{1}$$

where v is the complex current corresponding to horizontal velocity, K is the coefficient of turbulent viscosity, and f is the Coriolis parameter. The two parameters are assumed constant. Equation 1 is to be solved subject to the wind stress imposed at the sea surface

$$\left(K\frac{\partial v}{\partial z}\right)_{z=0}=\frac{\tau}{\rho} \tag{2A}$$

where τ is the wind stress and ρ is seawater density. Moreover, it is assumed that the stress vanishes at the lower boundary of the surface layer

$$\left(K\frac{\partial v}{\partial z}\right)_{z=-h}=0 \tag{2B}$$

If Eq. 1 is vertically integrated and corresponding boundary conditions (Eq. 2) are taken into account, it follows that

$$\frac{dV}{dt}+ifV=\frac{\tau}{\rho} \tag{3}$$

where the volume transport is

$$V=\int_{-h}^{0} v dz \tag{4}$$

The case of rotating wind stress

The wind stress is now assumed to be of the following form

$$\tau=A\exp(i\omega t)+B\exp(-i\omega t) \tag{5}$$

with A and B being arbitrary moduli. The form allows the wind stress to rotate CW ($A<B$), to be linearly polarized ($A=B$), or to rotate CCW ($A>B$). Equation 3 then results in

$$V=\frac{A}{i\rho(f+\omega)}\exp(i\omega t)+\frac{B}{i\rho(f-\omega)}\exp(-i\omega t) \tag{6}$$

Instructive are the cases in which the wind stress follows a circular path while rotating CW ($A=0$) or CCW ($B=0$), originally considered in (*12*). When the wind stress is rotating purely CW, the transport is to the right of the winds in the Northern Hemisphere at subinertial frequencies ($\omega<f$), there is resonance at the inertial frequency ($\omega=f$), and the transport is to the left of the winds in the Northern Hemisphere at superinertial frequencies ($\omega>f$). For the wind stress rotating purely CCW, the transport is reduced smoothly from the Ekman solution at subinertial frequencies to a smaller amplitude variations at superinertial frequencies, always deflected to the right of the winds and without resonant amplification at the inertial frequency. Equation 6 is also relevant for the case when the wind stress follows an elliptical path, either in a CW or in a CCW sense when both A and B are nonzero, with resonance occurring at the inertial frequency.

Although rich in content, Eq. 6 does not offer any information on the vertical variability of currents. For this, one has to return to Eq. 1 and corresponding boundary conditions (Eq. 2), which, with the wind forcing given above, leads to

$$v=\frac{A}{\rho K}\frac{D}{\pi(1+i)}\frac{\cosh\left[(1+i)\frac{\pi}{D}(z+h)\right]}{\sinh\left[(1+i)\frac{\pi}{D}h\right]}\exp(i\omega t)+\frac{B}{\rho K}\frac{D_1}{\pi(1+i)}\frac{\cosh\left[(1+i)\frac{\pi}{D_1}(z+h)\right]}{\sinh\left[(1+i)\frac{\pi}{D_1}h\right]}\exp(-i\omega t) \tag{7A}$$

at subinertial frequencies, and

$$v=\frac{A}{\rho K}\frac{D}{\pi(1+i)}\frac{\cosh\left[(1+i)\frac{\pi}{D}(z+h)\right]}{\sinh\left[(1+i)\frac{\pi}{D}h\right]}\exp(i\omega t)+\frac{B}{\rho K}\frac{D_2}{\pi(1-i)}\frac{\cosh\left[(1-i)\frac{\pi}{D_2}(z+h)\right]}{\sinh\left[(1-i)\frac{\pi}{D_2}h\right]}\exp(-i\omega t) \tag{7B}$$

at superinertial frequencies (*7*, *12*, *26*). The three depth scales, related to CCW rotation at all frequencies, CW rotation at subinertial frequencies, and CW rotation at superinertial frequencies, are, respectively

$$D=\pi\sqrt{\frac{2K}{f+\omega}},\ D_1=\pi\sqrt{\frac{2K}{f-\omega}},\ D_2=\pi\sqrt{\frac{2K}{\omega-f}} \tag{7C}$$

It is easy to verify that, for both subinertial and superinertial frequencies, vertical integration of Eq. 7 results in Eq. 6. Of interest are cases when the wind stress follows a circular path while rotating CW ($A=0$) or CCW ($B=0$). They show that, when the transport is directed to the right (left) of the wind, the currents are also directed to the right (left) of the wind and are, in some cases, spiraling with increasing depth. As implied by Eq. 7C, the vertical extent of wind-driven currents is limited by the Coriolis effect at low frequencies and by the frequency of wind variations at high frequencies, except when CW-rotating wind is resonantly coupled to inertial oscillations. Equation 7 shows that resonance is possible at the inertial frequency not only when the wind stress is rotating purely CW but also when it is following an elliptical path (i.e., when both A and $B\neq 0$).

Two special cases

To illustrate Eq. 7 in an easy-to-follow way, two special cases are considered. The first is based on the assumption that the depth of the constant density surface layer is much larger than the characteristic depth scales (i.e., $h >> D$, D_1, and D_2). Then, Eq. 7A and Eq. 7B reduce to

$$v=\frac{A}{\rho\sqrt{K(f+\omega)}}\exp\left(\frac{\pi}{D}z\right)\exp\left[i\left(\omega t+\frac{\pi}{D}z-\frac{\pi}{4}\right)\right]+\frac{B}{\rho\sqrt{K(f-\omega)}}\exp\left(\frac{\pi}{D_1}z\right)\exp\left[-i\left(\omega t-\frac{\pi}{D_1}z+\frac{\pi}{4}\right)\right] \tag{8A}$$

at subinertial frequencies, and

$$v=\frac{A}{\rho\sqrt{K(f+\omega)}}\exp\left(\frac{\pi}{D}z\right)\exp\left[i\left(\omega t+\frac{\pi}{D}z-\frac{\pi}{4}\right)\right]+\frac{B}{\rho\sqrt{K(\omega-f)}}\exp\left(\frac{\pi}{D_2}z\right)\exp\left[-i\left(\omega t+\frac{\pi}{D_2}z-\frac{\pi}{4}\right)\right] \tag{8B}$$

at superinertial frequencies (*11*, *13*, *14*). Note that there is no difference between dynamics in a semi-infinite ocean and in the surface layer of the ocean provided that the depth of the surface layer is much larger than the characteristic depth scales. The surface current is deflected by 45° to the right of the wind and spirals in the same direction in the case of CCW wind rotation at all frequencies and CW wind rotation at subinertial frequencies; conversely, the surface current is

deflected by 45° to the left of the wind and is spiraling in the same direction in the case of CW wind rotation at superinertial frequencies.

The second special case is novel in its derivation and is based on the assumption that the depth of the surface layer is much smaller than the characteristic depth scales (i.e., $h << D$, D_1, and D_2). Then, Eq. 7A and Eq. 7B reduce to slab-like flow in the mixed layer

$$v = \frac{A}{\rho h(f+\omega)}\exp\left[i\left(\omega t - \frac{\pi}{2}\right)\right] + \frac{B}{\rho h(f-\omega)}\exp\left[-i\left(\omega t + \frac{\pi}{2}\right)\right] \quad (9A)$$

at subinertial frequencies, and

$$v = \frac{A}{\rho h(f+\omega)}\exp\left[i\left(\omega t - \frac{\pi}{2}\right)\right] + \frac{B}{\rho h(\omega-f)}\exp\left[-i\left(\omega t - \frac{\pi}{2}\right)\right] \quad (9B)$$

at superinertial frequencies. It is of special interest that, now, the current is deflected by 90° to the right of the wind in the case of CCW wind rotation at all frequencies and CW wind rotation at subinertial frequencies, while it is deflected by 90° to the left of the wind in the case of CW wind rotation at superinertial frequencies.

Supplementary Materials

This PDF file includes:

Figs. S1 to S8

REFERENCES AND NOTES

1. V. W. Ekman, On the influence of the Earth's rotation on ocean-currents. *Ark. Mat. Astron. Fys.* **2**, 1–52 (1905).
2. R. T. Pollard, R. C. Millard, Comparison between observed and simulated wind-generated inertial oscillation. *Deep-Sea Res. Oceanogr. Abstr.* **17**, 813–821 (1970).
3. J. F. Price, R. A. Weller, R. R. Schudlich, Wind-driven ocean currents and Ekman transport. *Science* **238**, 1534–1538 (1987).
4. D. L. Rudnick, R. A. Weller, Observations of superinertial and near-inertial wind-driven flow. *J. Phys. Oceanogr.* **23**, 2351–2359 (1993).
5. T. K. Chereskin, Direct evidence for an Ekman balance in the California Current. *J. Geophys. Res.* **100**, 18261 (1995).
6. S. Elipot, R. Lumpkin, Spectral description of oceanic near surface variability. *Geophys. Res. Lett.* **35**, L05606 (2008).
7. S. Elipot, S. T. Gille, Ekman layers in the Southern Ocean: Spectral models and observations, vertical viscosity and boundary layer depth. *Ocean Sci.* **5**, 115–139 (2009).
8. Y.-D. Lenn, T. K. Chereskin, Observations of Ekman currents in the Southern Ocean. *J. Phys. Oceanogr.* **39**, 768–779 (2009).
9. J. O. Wenegrat, M. J. McPhaden, Wind, waves, and fronts: Frictional effects in a generalized Ekman Model. *J. Phys. Oceanogr.* **46**, 371–394 (2016).
10. K. J. Zoeppritz, Hydrodynamic problems in reference to the theory of ocean currents. *Philosoph. Mag.* **6**, 192–211 (1878).
11. M. Orlić, Wind-induced currents directed to the left of the wind in the northern hemisphere: An elementary explanation and its historical background. *Geofizika* **28**, 219–228 (2011).
12. J. Gonella, A rotary-component method for analysing meteorological and oceanographic vector time series. *Deep-Sea Res. Oceanogr. Abstr.* **19**, 833–846 (1972).
13. R. A. Weller, Observations of the velocity response to wind forcing in the upper ocean. *J. Geophys. Res.* **86**, 1969–1977 (1981).
14. P. D. Craig, Constant-eddy-viscosity models of vertical structure forced by periodic winds. *Cont. Shelf Res.* **9**, 343–358 (1989).
15. S. Elipot, S. T. Gille, Estimates of wind energy input to the Ekman layer in the Southern Ocean from surface drifter data. *J. Geophys. Res.* **114**, C06003 (2009).
16. J. R. Taylor, A. F. Thompson, Submesoscale Dynamics in the Upper Ocean. *Annu. Rev. Fluid Mech.* **55**, 103–127 (2023).
17. T. McKie, A. J. Lucas, J. MacKinnon, Submesoscale dynamics in the Bay of Bengal: Inversions and instabilities. *J. Geophys. Res. Oceans* **129**, e2023JC020563 (2024).
18. E. A. D'Asaro, The energy flux from the wind to near-inertial motions in the mixed layer. *J. Phys. Oceanogr.* **15**, 1043–1059 (1985).
19. M. H. Alford, J. A. MacKinnon, H. L. Simmons, J. D. Nash, Near inertial internal gravity waves in the ocean. *Ann. Rev. Mar. Sci.* **8**, 95–123 (2016).
20. S. T. Gille, S. G. Llewellyn Smith, N. M. Statom, Global observations of the land breeze. *Geophys. Res. Lett.* **32**, 10.1029/2004GL022139 (2005).
21. K. Athulya, M. S. Girishkumar, M. J. McPhaden, S. S. Kolukula, Seasonal variation of the land breeze system in the southwestern Bay of Bengal and its influence on air-sea interactions. *J. Geophys. Res.* **128**, e2022JC019477 (2023).
22. J. Neumann, On the rotation rate of the direction of sea and land breezes. *J. Atmos. Sci.* **34**, 1913–1917 (1977).
23. M. Orlić, B. Penzar, I. Penzar, Adriatic sea and land breezes: Clockwise versus anticlockwise rotation. *J. Appl. Meteorol.* **27**, 675–679 (1988).
24. J. E. Simpson, Diurnal changes in sea-breeze direction. *J. Appl. Meteorol.* **35**, 1166–1169 (1996).
25. S. T. K. Miller, B. D. Keim, R. W. Talbot, H. Mao, Sea breeze: Structure, forecasting, and impacts. *Rev. Geophys.* **41**, 1011 (2003).
26. J. M. Lilly, S. Elipot, A unifying perspective on transfer function solutions to the unsteady Ekman problem. *Fluids* **6**, 85 (2021).
27. C. N. K. Mooers, A technique for the cross spectrum analysis of pairs of complex-valued time series, with emphasis on properties of polarised components and rotational invariants. *Deep-Sea Res. Oceanogr. Abstr.* **20**, 1129–1141 (1973).
28. E. Rodríguez, M. Bourassa, D. Chelton, J. T. Farrar, D. Long, D. Perkovic-Martin, R. Samelson, The winds and currents mission concept. *Front. Mar. Sci.* **6**, 00438 (2019).
29. H. Torres, A. Wineteer, P. Klein, T. Lee, J. Wang, E. Rodriguez, D. Menemenlis, H. Zhang, Anticipated capabilities of the ODYSEA wind and current mission concept to estimate wind work at the air–sea interface. *Remote Sens. (Basel)* **15**, 3337 (2023).
30. The National Academy of Sciences, Engineering, and Medicine, *Thriving on Our Changing Planet: A Decadal Strategy for Earth Observational From Space* (The National Academy Press, USA, 2018).
31. R. Venkatesan, V. R. Shamji, G. Latha, S. Mathew, R. R. Rao, A. Muthiah, M. A. Atmanand, In situ ocean subsurface time-series measurements from OMNI buoy network in the Bay of Bengal. *Curr. Sci.* **104**, 1166–1177 (2013).
32. R. B. Stull, *Practical Meteorology: An Algebra-Based Survey of Atmospheric Science* (University of British Columbia, 2015).
33. C. W. Fairall, E. F. Bradley, J. E. Hare, A. A. Grachev, J. B. Edson, Bulk parameterization on air-sea fluxes: Updates and verification for the COARE algorithm. *J. Climate* **16**, 571–591 (2003).
34. C. Mears, T. Lee, L. Ricciardulli, X. Wang, F. Wentz, RSS Cross-Calibrated Multi-Platform (CCMP) monthly ocean vector wind analysis on 0.25 deg grid, version 3.0, Remote Sensing Systems (2022); https://doi.org/10.56236/RSS-uv1m30.
35. R. K. Jha, T. V. S. Udaya Bhaskar, "Data-Interpolating Variational Analysis (DIVA) method for the generation of argo data gridded products" (Tech. Rep. ESSO-INCOIS-TPG-TR0, 2020), pp. 1–46.
36. R. E. Thomson, W. J. Emery, *Data Analysis Methods in Physical Oceanography* (Elsevier, Ed. 3, 2014).
37. D. L. Gilman, F. J. Fuglister, J. M. Mitchell, On the power spectrum of "red noise". *J. Atmos. Sci.* **20**, 182–184 (1963).
38. S. Mohanty, "Generation and propagation of internal tides off the east coast of India and over the Andaman Sea using a numerical model," thesis, Indian Institute of Technology, Delhi (2018).
39. J. Marshall, A. Adcroft, C. Hill, L. Perelman, C. Heisey, A finite-volume, incompressible Navier Stokes model for studies of the ocean on parallel computers. *J. Geophys. Res.* **102**, 5753–5766 (1997).
40. B. Sindhu, I. Suresh, A. S. Unnikrishnan, N. V. Bhatkar, S. Neetu, G. S. Michael, Improved bathymetric datasets for the shallow water regions in the Indian Ocean. *J. Earth Syst. Sci.* **116**, 261–274 (2007).
41. J. Smagorinsky, General circulation experiments with the primitive equations: I. The basic experiment. *Mon. Weather Rev.* **91**, 99–164 (1963).
42. W. G. Large, J. C. McWilliams, S. C. Doney, Oceanic vertical mixing: A review and a model with a nonlocal boundary layer parameterisation. *Rev. Geophys.* **32**, 363–403 (1994).
43. R. A. Locarnini, A. V. Mishonov, J. I. Antonov, T. P. Boyer, H. E. Garcia, O. K. Baranova, M. M. Zweng, C. R. Paver, J. R. Reagan, D. R. Johnson, M. Hamilton, D. Seidov, *World Ocean Atlas 2013, Volume 1: Temperature* (NOAA Atlas NESDIS 73, 2013), pp. 1–40.
44. G. D. Egbert, S. Y. Erofeeva, Efficient inverse modeling of barotropic ocean tides. *J. Atmos. Oceanic Tech.* **19**, 183–204 (2002).

Acknowledgments: We thank the anonymous reviewers for thoughtful and constructive comments on an earlier version of this manuscript. The moored buoy data were collected as part of the Ocean Moored buoy Network for the Northern Indian Ocean (OMNI) maintained by MoES-NIOT, Chennai. Thanks to S. Mohanty, Scientist, IIRE, for providing MITgcm model data to facilitate the analysis. PMEL contribution no. 5584. INCOIS contribution no. 535. **Funding:** M.J.M. was supported by NOAA/PMEL and NOAA's Global

Ocean Monitoring and Observing Program. M.O. received support through grant no. 20286578 provided to the Andrija Mohorovičić Geophysical Institute by the Croatian Ministry of Science and Education. K.A. acknowledges the support provided by the Council of Scientific & Industrial Research (CSIR) Research Fellowships as part of the PhD program. **Author contributions:** M.J.M. conceived the paper, coordinated the study, and wrote the first version of the manuscript. K.A. and M.S.G. analyzed the datasets and generated graphical presentations. M.O. provided theoretical underpinnings to support the analysis and historical context for the study. All authors discussed the results, refined the concepts, and contributed to writing the final version of the paper. **Competing interests:** The authors declare that they have no competing interests. **Data and materials availability:** OMNI mooring data are available at https://incois.gov.in/portal/datainfo/buoys.jsp. CCMP version 2.0 vector wind analyses are produced by Remote Sensing Systems with data available at www.remss.com. The gridded Argo temperature and salinity product is produced and distributed by INCOIS with data accessible from https://las.incois.gov.in/. All other data needed to evaluate the conclusions in the paper are present in the paper and/or the Supplementary Materials.

Submitted 11 June 2024
Accepted 10 October 2024
Published 13 November 2024
10.1126/sciadv.adr0282